Published online 7 December 2021

Nucleic Acids Research, 2022, Vol. 50, No. 4 ***e24***
https://doi.org/10.1093/nar/gkab1185

Analysis of subcellular transcriptomes by RNA proximity labeling with Halo-seq

Krysta L. Engel[1], Hei-Yong G. Lo[1,2], Raeann Goering[1,2], Ying Li[3], Robert C. Spitale[4,5,*] and J. Matthew Taliaferro[1,2,*]

[1]Department of Biochemistry and Molecular Genetics, University of Colorado Anschutz Medical Campus, Aurora, CO, USA, [2]RNA Bioscience Initiative, University of Colorado Anschutz Medical Campus, Aurora, CO, USA, [3]Department of Chemistry, Hong Kong University, [4]Department of Pharmaceutical Sciences, University of California Irvine, Irvine, CA, USA and [5]Department of Chemistry, University of California Irvine, Irvine, CA, USA

Received July 01, 2021; Revised October 26, 2021; Editorial Decision November 12, 2021; Accepted November 16, 2021

ABSTRACT

Thousands of RNA species display nonuniform distribution within cells. However, quantification of the spatial patterns adopted by individual RNAs remains difficult, in part by a lack of quantitative tools for subcellular transcriptome analysis. In this study, we describe an RNA proximity labeling method that facilitates the quantification of subcellular RNA populations with high spatial specificity. This method, termed Halo-seq, pairs a light-activatable, radical generating small molecule with highly efficient Click chemistry to efficiently label and purify spatially defined RNA samples. We compared Halo-seq with previously reported similar methods and found that Halo-seq displayed a higher efficiency of RNA labeling, indicating that it is well suited to the investigation of small, precisely localized RNA populations. We then used Halo-seq to quantify nuclear, nucleolar and cytoplasmic transcriptomes, characterize their dynamic nature following perturbation, and identify RNA sequence features associated with their composition. Specifically, we found that RNAs containing AU-rich elements are relatively enriched in the nucleus. This enrichment becomes stronger upon treatment with the nuclear export inhibitor leptomycin B, both expanding the role of HuR in RNA export and generating a comprehensive set of transcripts whose export from the nucleus depends on HuR.

INTRODUCTION

In species ranging from yeast to mammals, many RNA species are distributed asymmetrically within cells (1–4). Mislocalization of these RNAs often results in cellular or organismal phenotypes, underscoring the importance of the process (1,5,6). RNAs are often trafficked to their destination through the action of RNA binding proteins (RBPs) that bind specific *cis* sequence elements, usually in the 3′ UTR, and mediate transport (7,8). However, for most localized RNAs the identity of the *cis*-elements and *trans*-acting RBPs are unknown.

Historically, much of the work done to study RNA localization has used imaging-based approaches (9). With these experiments, the location of RNA molecules within cells can be directly visualized. However, with the exception of new multiplexed techniques (10,11), these imaging experiments are generally limited to the interrogation of one or a few transcript species at a time. Further, short RNAs including snRNAs and snoRNAs are generally not compatible with the hybridization-based techniques used in many RNA visualization experiments.

More recently, techniques have been developed that isolate and characterize subcellular transcriptomes using high-throughput sequencing. In particular, transcriptomes of neuronal cell bodies and processes have been extensively probed in this way. These studies have relied on the elaborate, branched morphologies of neurons that facilitate their physical, mechanical separation into subcellular fractions and have identified hundreds of RNAs that are enriched in processes (12–15).

Asymmetric RNA distributions are also prevalent throughout cell types that lack morphologies with long, thin processes typical of neurons. Until recently, technical limitations have precluded the transcriptome-wide study of RNA trafficking in these cell types. New techniques have been developed that rely on RNA proximity to protein markers of specific subcellular locations (16–19). These techniques initially label localized (i.e. protein-marker-proximal) RNA in living cells. Labeling is achieved through the enzymatic production of reactive oxygen species, which diffuse from their point of generation (i.e. the localized protein marker) and leave marks on nearby RNA molecules.

*To whom correspondence should be addressed. Tel: +1 303 724 3274; Fax: +1 303 724 3215; Email: matthew.taliaferro@cuanschutz.edu
Correspondence may also be addressed to Robert C. Spitale. Email: rspitale@uci.edu

These marks then facilitate purification of the labeled, localized RNA away from bulk total RNA. Localized RNAs are then identified as those that are more abundant in the labeled RNA than the total RNA.

Although these proximity labeling techniques have been used to probe the RNA contents of various subcellular locations (16,18,19), their enzymatic approaches to radical generation may limit the amount of radicals produced and therefore the sensitivity of RNA labeling. A nonenzymatic technique for radical generation using a light-sensitive Halo ligand fluorophore, dibromofluorescein (DBF) was recently described (20,21), but its ability to provide comprehensive characterization of subcellular transcriptomes has not been tested. Here, we demonstrate that DBF-mediated RNA proximity labeling can be used to efficiently characterize subcellular transcriptomes and derive mechanistic insights into factors controlling their composition.

MATERIALS AND METHODS

Creation of transgenic cell lines expressing Halo fusion proteins

HeLa cell lines were created by integrating a plasmid containing the Halo fusion using *cre*/*lox* recombination (26). HeLa cells containing a single *loxP* cassette were plated in a six-well plate and co-transfected with 2000 ng of a plasmid containing the Halo fusion and a puromycin selectable marker and 100 ng of a plasmid, pBT140, that expressed *Cre* recombinase. pBT140 was a gift from Liqun Luo (Addgene plasmid # 27493; http://n2t.net/addgene:27493;RRID:Addgene_27493) (66).

The transfection was carried out using Lipofectamine 2000 (Thermo Scientific) according to the manufacturer's instructions. Forty-eight hours after transfection, the cells were incubated with 5 μg/ml puromycin in order to select for integrants. Approximately 2 weeks after transfection, a stable population of integrants had been selected.

The plasmid containing the Halo fusion also contained a reverse tetracycline-controlled transactivator (rtTA), allowing the expression of Halo fusions to be controlled in a doxycycline-dependent manner. To induce expression of the Halo fusion, selected cell lines were incubated with 1 μg/ml doxycycline for 48 h prior to performing experiments.

The H2B fusion was expressed as a C-terminal Halo fusion (i.e. H2B-Halo) while the p65 and fibrillarin fusions were expressed as N-terminal Halo fusions (i.e. Halo-p65 and Halo-fibrillarin).

Synthesis of Halo-DBF ligand

Halo-DBF was synthesized as previously described (20). We are currently in discussions with commercial providers about their ability to produce this ligand in order to better serve the community.

Validation of subcellular localization of Halo fusion proteins

To verify that the transgenic Halo fusion proteins were targeted to the correct subcellular location, the location of the fusions were visualized using a fluorescent Halo ligand. Cells were seeded on poly-D-lysine-coated coverslips and incubated with 1 μg/ml doxycycline for 48 h. The media was then removed and the cells were washed one time with PBS. Cells were then fixed by incubating them in 2% formaldehyde for 30 min at room temperature. The cells were then washed with PBS again, and fluorescent Halo ligand (Janiela Fluor 646 (Promega), 25 nM in PBS) was added. The cells were incubated in the Halo ligand solution for 30 min at room temperature then washed three times with PBS for 5 min each. DAPI was then added to a concentration of 100 ng/ml for 10 min, and the cells were washed again with PBS. The coverslips were then mounted and imaged, usually at 60× magnification, using a Deltavision Elite widefield fluorescence microscope (GE).

In-cell alkynylation of Halo-proximal RNAs

Cells were grown in 10 cm or 15 cm dishes, and the expression of Halo fusion proteins was induced with 1 μg/ml doxycycline for 48 h. Cells were then washed with PBS and incubated with 1 μM DBF halo ligand (in HBSS) at 37°C for 15 min. For negative control samples, the DBF halo ligand was omitted.

Cells were then washed with complete media and incubated at 37°C twice for 10 min each. Propargylamine (Sigma, 1 mM in HBSS) was then added, and the cells were incubated for 5 min at 37°C. Following the incubation, cells were then irradiated with green light for 5 min from a 100 W LED flood light (USTELLAR UT88831-RGB-US). Dishes were sandwiched between two flood lights in a dark enclosed space so that they were illuminated from above and below. The light above the dish was suspended ∼10 cm from the dish. Total RNA was then isolated from the cells using Trizol (Ambion) following the manufacturer's instructions with the addition of a homogenization step in which the cells in Trizol solution are repeatedly forced through a 20 gauge needle 10 times.

The RNA was then DNase treated using DNase I (Thermo Scientific) for 30 min at 37°C. RNA was then again recovered using Trizol, and the final pellet was resuspended in water to a concentration higher than ∼300 ng/ul. This ensures the ability to have the correct concentration in Click reactions downstream. Typical total RNA yields were 25–100 μg if starting with a 10 cm dish and 300–700 μg if starting with a 15 cm dish.

In vitro biotinylation of alkynylated RNAs using Click chemistry

Typically, ∼50–100 μg of total RNA was used in the Click reaction. The Click reaction contained 10 mM Tris pH 7.5, 2 mM biotin azide (Click Chemistry Tools), 10 mM sodium ascorbate made fresh (Sigma), 2 mM THPTA (Click Chemistry Tools), and 100 μM copper sulfate. The reaction was incubated for 30 min in the dark at 25°C. The reaction was then cleaned up using a Quick RNA Mini kit (Zymo Research) for small scale biotinylation tests (<10 μg RNA), or through standard ethanol precipitation with sodium acetate for larger amounts of RNA (>10 μg). RNA was then eluted and resuspended to 1 μg/μl in 50 mM NaCl.

Streptavidin purification of biotinylated RNA

Typically, between 50 and 100 μg of RNA at 1 μg/μl from the Click reaction was then carried forward for streptavidin pulldowns. 25–50 μl of streptavidin-coated magnetic beads (Pierce PI88816) were used depending on the known amount of labeled RNA present in the reaction. Specifically, we used 1 μl beads per 1 μg total RNA for Halo-p65 and Halo-fibrillarin, and 1 μl beads: per 2 μg RNA for H2B. The beads were washed 3 times in B&W buffer (5 mM Tris pH 7.5, 0.5 mM EDTA, 1M NaCl, 0.1 Tween 20), 2 times in solution A (0.1 M NaOH, 50 mM NaCl), and 1 time in solution B (100 mM NaCl). The beads were resuspended in an appropriate amount of NaCl to allow for 50 mM final concentration after the addition of the desired amount of RNA to equal 1 μg/μl. The RNA from the Click reaction was then added to the beads, and the beads were rotated for 2 h at 4°C. The beads were then washed 3 times for 5 min each in B&W buffer with rotation at room temperature.

RNA was then recovered from the beads using Trizol. First, the beads were resuspended in 50 μl PBS. 150 μl of Trizol was then added, and this mixture was incubated for 5–10 min at 37°C. The eluted RNA (without the magnetic beads) was then recovered from this mixture using a Direct-Zol kit (Zymo Research) following the manufacturer's instructions and eluted in 10 μl of water. Depending on the location of the Halo fusion protein, typically between 0.5% and 5% of the input RNA was recovered by streptavidin pulldown.

RNA dot blot

RNA biotinylation, both before and after the streptavidin pulldown, was assessed using an RNA dotblot. A 5 cm × 5 cm piece of Hybond-N + membrane (GE) was wet with 2× SSC for 1 min. This was then allowed to dry for 15 min. RNA samples, typically around 5 μg, were then spotted on the membrane and allowed to dry for 30 min. The dried blots were then crosslinked twice to the membrane using 120 000 μJ/cm^2 on a Stratalinker UV crosslinker (Stratagene).

To stain for total RNA, the blot was then incubated in 1% methylene blue for 10 min and destained using deionized water. The membrane was then blocked using 5% BSA for 30 min and washed 3 times in PBST (PBS + 0.01% Tween). Biotinylated RNA was then detected using streptavidin-HRP (Abcam ab7403) at a dilution of 1 to 20 000 in 3% BSA by addition to the membrane with rocking overnight at 4°C. The membrane was then washed 3 times for 10 min each in PBST at room temperature. Streptavidin–HRP was then detected using standard HRP chemiluminescent reagents (Advansta) and visualized using chemiluminescent imaging on a Sapphire molecular imager (Azure Biosystems).

Library preparation and high-throughput sequencing

rRNA-depleted RNAseq libraries were prepared using an RNA HyperPrep Kit (KAPA/Roche). 100 ng of RNA were put into the beginning of the library prep protocol, and 14 PCR cycles were used to amplify the library at the end.

Libraries were sequenced using paired end sequencing (2 × 150 bp) on a NovaSeq high-throughput sequencer (Illumina) at the University of Colorado Genomics Core Resource. Typically, between 20 and 40 million read pairs were sequenced for each sample.

Analysis of RNAseq data to identify genes enriched in streptavidin pulldown

Transcript abundances in RNAseq data were quantified using Salmon (27) and a human genome annotation retrieved from GENCODE (www.gencodegenes.org, GENCODE 28). Gene abundances were then calculated from these transcript abundances using tximport (28), and genes whose abundance in input and streptavidin-pulldown samples were identified using DESeq2 (29). In these analyses, genes were required to have at least 5 counts in all samples tested in a particular analysis. In order to be called enriched or depleted in a given sample, a gene was required to have an adjusted *P*-value of <0.05 and an absolute $\log_2$ fold change of at least 0.5.

Analysis of unspliced transcripts in RNAseq data

In order to quantify the relative abundances of spliced and unspliced (all introns remaining) versions of transcripts, a custom fasta file was supplied to Salmon which contained two versions of every transcript, one with all introns remaining and one with all introns removed. The custom fasta file was generated using this script: https://github.com/rnabioco/rnaroids/blob/master/src/add_primary_transcripts.py. Salmon then assigned reads competitively to these transcripts. For each gene, the ratio of abundances of unspliced and spliced transcripts was then calculated.

Definition of AU-rich elements within transcripts

AU-rich element locations were downloaded from the AU-rich element database (59). AU-rich elements within 3′ UTRs were used for analysis.

In situ Click reaction using Cy5-azide

To visualize the subcellular location of DBF-proximal alkynylated molecules *in situ*, cell growth and Halo fusion induction were performed as described above with the exception that cells were grown on poly-D-lysine-coated coverslips. The in-cell alkynylation of DBF-proximal molecules was also performed as described above. Then, instead of lysing cells with Trizol to recover RNA, cells were washed with PBS 3 times and fixed by incubating them in fixation buffer (3.7% formaldehyde, 0.1% Triton in PBS) for 30 min at room temperature. Cells were then washed twice for 5 min each in PBS.

The Click reaction was then performed by incubating cells with 100 μl Click buffer (100 μM copper sulfate, 2 mM THPTA, 10 mM fresh sodium ascorbate, 10 μM Cy5 picolyl azide (Click Chemistry Tools 1171-1)) for 1 h at 37°C in the dark. As two separate controls, samples in which the DBF had been left out during the alkynylation reaction and the Cy5 had been left out of the Click buffer were used. Following the Click reaction, the coverslips were

washed three times for 5 min each in wash buffer (0.1% Triton, 1 mg/ml BSA in PBS). Coverslips were then incubated in DAPI buffer (100 ng/ml DAPI in wash buffer) for 30 min at 37°C and then washed twice with wash buffer for 5 min each. The coverslips were then mounted and imaged using a Deltavision Elite widefield fluorescence microscope (GE).

Treatment with Leptomycin B

Cells were treated with 40 ng/ml leptomycin B (LMB) for 15 h prior to the beginning of the Halo-seq protocol. To verify the activity of leptomycin B and our conditions, the localization of the Halo-p65 fusion was monitored. The cytoplasmic localization of p65 is sensitive to LMB (67) (Figure 5A). Accordingly, the normally cytoplasmically localized Halo-p65 fusion became localized to the nucleus following LMB treatment (Figure 5A).

Identification of RNAs whose subcellular localization was sensitive to LMB

Halo-seq using a histone H2B Halo fusion was performed in the presence and absence of LMB, generating four conditions: input samples with and without LMB and pulldown samples with and without LMB. To identify genes whose pulldown to input ratio changed between the LMB treated and untreated samples, the software package Xtail was used (58). Xtail is designed for the analysis of ribosome profiling data and identification of genes whose ribosome occupancy changes across conditions. Ribosome profiling data is the ratio of two gene expression values, one drawn from ribosome footprints and the other drawn from bulk RNA. Xtail identifies genes whose ratio changes between two conditions. The analysis of Halo-seq data is structurally similar as it is also a ratio of gene expression values, one from an input sample and another from a pulldown sample. We therefore used Xtail to identify genes whose ratio (i.e. nuclear enrichment) changed between LMB treated and untreated samples.

Comparison of RNA labeling with miniSOG2

Cells stably expressing HA-miniSOG2 were treated alongside cells stably expressing Halo-HA. The expression of miniSOG2 and Halo-HA was induced with 1 μg/ml doxycycline for 48 h. Cells were then washed with PBS. Halo-expressing cells were then incubated with Halo-DBF ligand at 37°C for 5 min, and both cell lines were then incubated with propargylamine (Sigma, 1 mM in HBSS) at 37°C for 5 min. Following the incubation, cells were irradiated with blue light (for miniSOG2) or green light (for Halo-DBF) for a total of 10 min with a 100 W LED flood light (USTELLAR). Dishes were sandwiched between two flood lights so that they were illuminated from above and below. The light above the dish was suspended ∼10 cm from the dish. Total RNA was then isolated from the cells using Trizol (Ambion) following the manufacturer's protocol after homogenization with a 20 gauge needle 10 times. RNA was biotinylated following the protocols described above.

Comparison of RNA labeling with APEX2

A cell line was created expressing a Halo-APEX2 fusion protein to ensure equal expression of HaloTag domain and APEX2 protein. RNA labeling with APEX2 was done alongside Halo-DBF-mediated labeling (described above). Expression of the Halo-APEX2 fusion protein was induced with 1 μg/ml of doxycycline for 48 h. To label RNA with the APEX2 protein, cells were washed with PBS and then incubated with HBSS containing 0.5 mM biotin phenol (APExBIO A8011) for 30 min at 37°C. Cells were then washed in PBS and either treated with hydrogen peroxide at 1 mM in HBSS or plain HBSS (control) for 7 min at 37°C (labeling of compared RNA using the Halo-DBF method was also subject to 7 min of exposure to green light). The reaction was quenched in quenching buffer containing 5 mM Trolox, 10 mM sodium ascorbate and 10 mM sodium azide in PBS. To fully quench the reaction, cells were washed three times in quenching buffer, with 3 min between each wash. Total RNA was isolated from the cells using Trizol (Ambion) after homogenization with a 20 gauge needle. After DNAse treatment, RNA was then directly blotted onto an RNA dotblot.

Comparison with APEX-seq data

APEX-seq RNAseq data was downloaded from the Gene Expression Omnibus (GSE116008) and processed to calculate transcript and gene abundances as above. Since the libraries were produced using poly-A enrichment of RNA, only protein-coding and lncRNA genes were used for comparisons to Halo-seq data.

Comparison with CeFra-seq data

CeFra-seq RNAseq data was downloaded from the ENCODE portal (www.encodeproject.org). Transcript and gene abundances from rRNA-depleted libraries were calculated using Salmon, tximport, and DESeq2 as outlined above. While Halo-seq enrichments were calculated as a gene's abundance in the streptavidin pulldown divided by its abundances in the input to the pulldown, CeFra-seq enrichments were calculated as a gene's abundance in the biochemically defined fraction (e.g. cytosol or nucleus) divided by its abundance in the total RNA samples.

RESULTS

Halo-seq allows in situ alkynylation of spatially resolved RNA populations

Halo-seq uses HaloTag domains genetically fused to a protein that specifically marks the subcellular location of interest. HaloTags are protein domains that covalently bind to a class of small molecules called Halo ligands (22). If a Halo ligand is added to cells expressing a spatially restricted protein containing a HaloTag, the ligand will therefore be similarly restricted.

The Halo ligand used in Halo-seq is dibromofluorescein (DBF). DBF generates singlet oxygen radicals when irradiated with green light (20,21). The high reactivity of these radicals restricts their diffusion from the DBF source

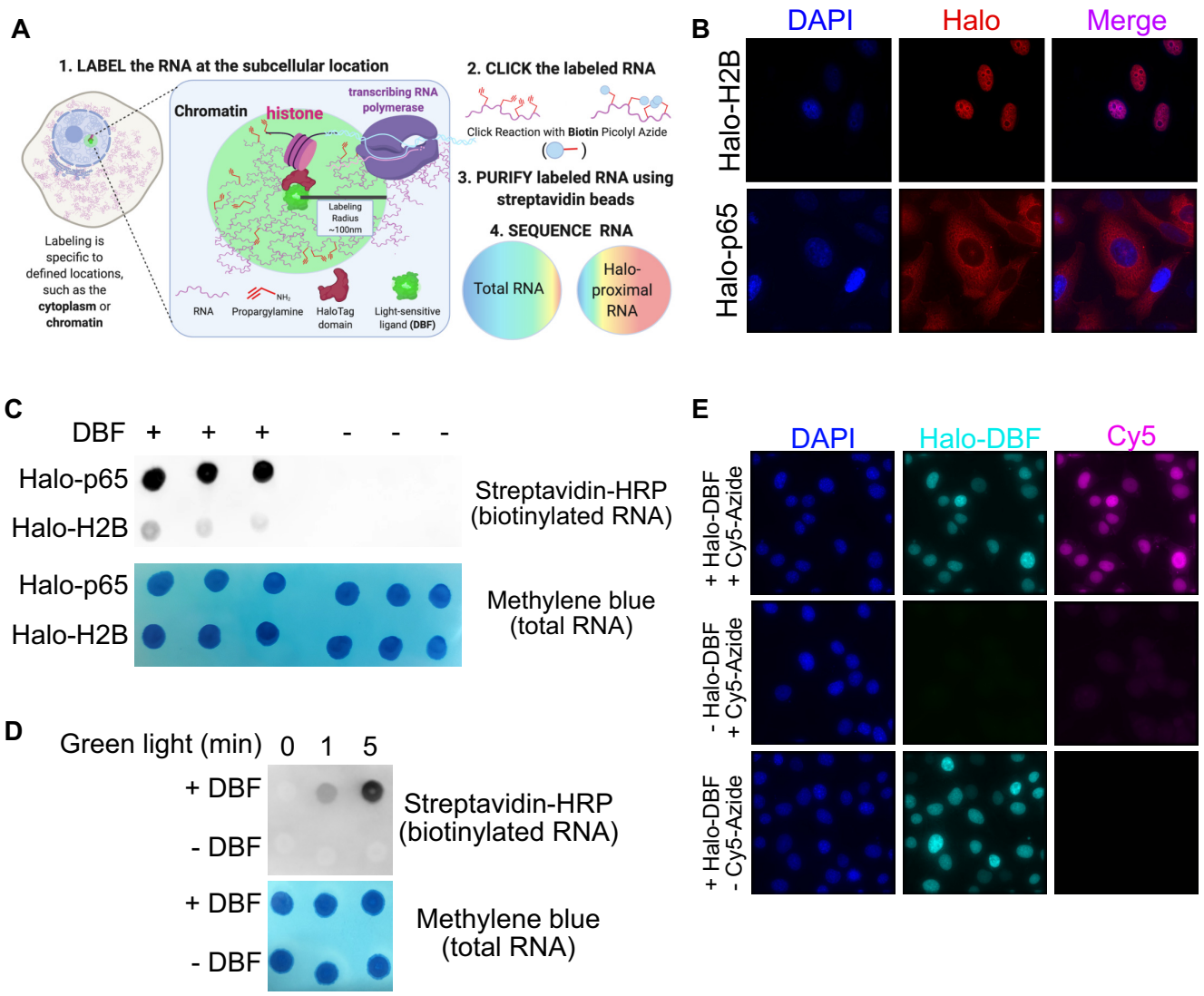

Figure 1. Halo-seq facilitates the biotinylation of RNA transcripts in proximity to spatially restricted Halo-DBF molecules. (**A**) Overview of the Halo-seq procedure. A HaloTag protein domain is genetically fused to a protein which localizes to a subcellular location of interest. Because Halo ligands specifically bind HaloTags, this also spatially restricts a DBF Halo ligand. When irradiated with green light, DBF emits oxygen radicals that label nearby RNAs, resulting in their alkynylation. Alkynykated RNAs are substrates for *in vitro* biotinylation using 'Click' chemistry, which allows the localized RNAs to be separated from the bulk RNA sample with streptavidin pulldown, and quantified using high-throughput sequencing. (**B**) HaloTag protein domains fused to histone H2B and p65 are localized to chromatin, and the cytoplasm, respectively. HaloTag domains are visualized through the addition of a Halo ligand fluorophore. (**C**) RNA samples taken from cells expressing Halo fusions can be biotinylated *in vitro*, and this biotinylation is dependent upon the addition of a DBF Halo ligand to cells. (**D**) RNA samples taken from cells expressing Halo-p65 fusion. Cells were treated with DBF Halo ligand and then exposed to green light for 0, 1 or 5 min. RNA labeling, as assayed by the detection of biotinylated RNA following *in vitro* Click reactions, required both DBF and exposure to green light. (**E**) Alkynylated molecules can be visualized *in situ* by fusing them with fluorophores (e.g. Cy5-azide) using Click chemistry. Alkynylated molecules are restricted to the nucleus in cells containing H2B-Halo. They are only detectable in cells treated with both DBF and Cy5-azide, demonstrating the ability of HaloTag-restricted DBF to induce alkynylation of biomolecules.

to a radius of ∼100 nm (Figure 1A) (20,23,24). When these radicals react with an RNA base within this 100 nm radius, the base becomes oxidized and prone to nucleophilic attack by a cell-permeable, alkyne-containing nucleophile, propargylamine (PA). RNA molecules within 100 nm of a DBF molecule are therefore selectively alkynylated. Importantly, this alkynylation occurs while the cell is alive and intact, providing confidence that the alkynylated RNA molecules are spatially coincident with the region of interest.

Following the in-cell alkynylation, cells are lysed and total RNA is collected. Alkynylated molecules are efficient substrates for *in vitro* Cu(I)-catalyzed azide-alkyne cycloaddition (CuACC) 'Click' chemistry in which alkyne-containing molecules and azide-containing molecules are linked (25). Reaction with biotin-azide therefore selectively biotinylates RNA molecules that were in close proximity to DBF, facilitating their isolation with streptavidin and analysis by high-throughput sequencing. By comparing RNA abundances in total RNA samples and streptavidin-purified

samples, transcripts that were enriched in the subcellular region of interest are identified.

To test the ability of Halo-seq to purify and quantify subcellular transcriptomes, we restricted HaloTag domains to chromatin and the cytoplasm. These HaloTag localizations were achieved by fusing to histone H2B and p65, a cytoplasmically-localized NF-kappa B subunit, respectively. Restriction of Halo and DBF to these locations was previously demonstrated to enable RNA tagging with high spatial resolution as assayed by RT-qPCR (20,21). We reasoned that since the RNA contents of nucleic and cytoplasmic compartments have been well-characterized, we would be able to easily assay the accuracy of the Halo-seq procedure. Using *cre*-mediated recombination, we integrated a single, doxycycline-inducible copy of these fusion constructs into the genomes of HeLa cells that contained a single *lox*P recombination cassette (26). We then verified the proper subcellular localization of the fusion proteins by visualizing them with fluorescent Halo ligands (Figure 1B).

We next assayed the ability of Halo-seq to produce biotinylated RNA using an RNA dot blot in which biotinylated RNA is detected using streptavidin-HRP. We found that RNA samples from both the Halo-p65 and H2B-Halo expressing lines could be efficiently biotinylated (Figure 1C). This biotinylation was dependent upon the addition of DBF to the cells, indicating that RNA biotinylation is dependent on the Halo-seq procedure and not due to an endogenous activity. Since all samples were subjected to the same procedures *in vivo* and *in vitro*, this also indicates that the level of biotinylation via any background labeling *in vitro* is very low.

To assess the dependence of the alkynylation reaction on light activation, we performed the RNA labeling reaction in DBF-treated Halo-p65-expressing cells using varying amounts of exposure to green light (Figure 1D). When the cells were not exposed to green light, we detected very little RNA labeling. We detected moderate amounts of RNA labeling following green light exposure for 1 min, and substantial amounts of RNA labeling following green light exposure for 5 min. We conclude, therefore, that the labeling reaction requires activation by light.

Next, we sought to visualize the localization of alkynylated molecules in cells following treatment with DBF and excitation with green light. This can be accomplished by fixing the cells after alkynylation and performing the Click reaction *in situ* with an azide coupled to a fluorescent molecule. With this approach, we found that the nucleus of cells expressing H2B-Halo was rich in alkynes, as evidenced by strong nuclear Cy5-azide signal that was dependent on the addition of DBF (Figure 1E). Performing similar experiments with cells expressing Halo-p65 and Halo-fibrillarin fusions showed Cy5-azide signal in the cytoplasm and nucleolus, respectively, that was also dependent upon the addition of DBF (Supplementary Figure S1A,B). Overall, these results demonstrate that our approach is high-resolution and enables imaging based analysis of tagging.

Quantification of subcellular transcriptomes with Halo-seq

We then characterized nuclear and cytoplasmic transcriptomes by comparing RNA abundances in samples taken before and after streptavidin-pulldowns. RNAs that were enriched at the subcellular location of interest should be enriched in the streptavidin-pulldown sample relative to the input sample. For each condition, either three or four biological replicates were used. We prepared rRNA-depleted libraries for high-throughput sequencing, quantified transcript expression in the resulting data using Salmon (27), and collapsed the data to gene-level abundances with tximport (28). Genes whose abundances were significantly different between input and streptavidin-pulldown samples were identified using DESeq2 (29).

Principal component analysis of gene expression profiles revealed that input and pulldown samples were markedly different from each other in both the H2B and p65 experiments (Supplementary Figure S1C, D), suggesting that the Halo-seq procedure reproducibly isolated distinct RNA populations. Hundreds of genes were both enriched and depleted in the pulldowns from the H2B and p65 experiments (Figure 2A, B, Supplementary Tables S1 and S2), further indicating that Halo-seq can identify distinct nuclear and cytoplasmic transcriptomes.

We then further analyzed the H2B and p65 samples, paying special attention to RNA species and classes known to be enriched in either the nuclear or cytoplasmic compartments. Several RNA species, including the 7SK RNA, RNase P, and TERC, function primarily in the nucleus and are known to accumulate there (30–32). Accordingly, all of these RNAs were enriched in the pulldown of the H2B experiment and depleted in the pulldown of the p65 experiment (Figure 2C). Conversely, GAPDH mRNA is known to accumulate to a higher relative level in the cytoplasm than in the nucleus, and this was also reflected in the relative enrichments from the H2B and p65 experiments (Figure 2C). Small nucleolar RNAs (snoRNAs), a class of small noncoding RNAs involved in ribosomal RNA maturation and ribosome biogenesis, are primarily localized to the nucleolus (33). Accordingly, the snoRNA *SNORA68* was depleted in both the H2B and p65 pulldowns. Because the nucleus and nucleolus are in close proximity to each other yet H2B is excluded from the nucleolus, this indicates that RNA labeling with Halo-seq displays a high degree of spatial selectivity.

To generalize these results, we then compared enrichment for classes of RNAs. Long noncoding RNAs (lncRNAs) are generally depleted from the cytoplasm (34,35). In agreement with this, we observed that lncRNAs, as a class, were significantly less enriched in the p65 pulldown than in the H2B pulldown (Figure 2D). Similarly, snRNAs are enriched in the nucleus (36), and Halo-seq found them to be enriched in the H2B pulldown and depleted in the p65 pulldown. This contrasts with protein-coding RNAs, which as a class spend substantial time in both the nuclear and cytoplasmic compartments. These RNAs were equally enriched in the H2B and p65 pulldowns.

We then turned to the quantification of dynamically processed RNA species. Most protein-coding human RNAs undergo splicing in the nucleus before export to the cytoplasm, and for many RNAs this splicing happens cotranscriptionally (37). We therefore wondered if we could observe an enrichment for unspliced pre-mRNA in close proximity to chromatin via the H2B pulldown. For each gene, we quantified the relative abundance of spliced and unspliced

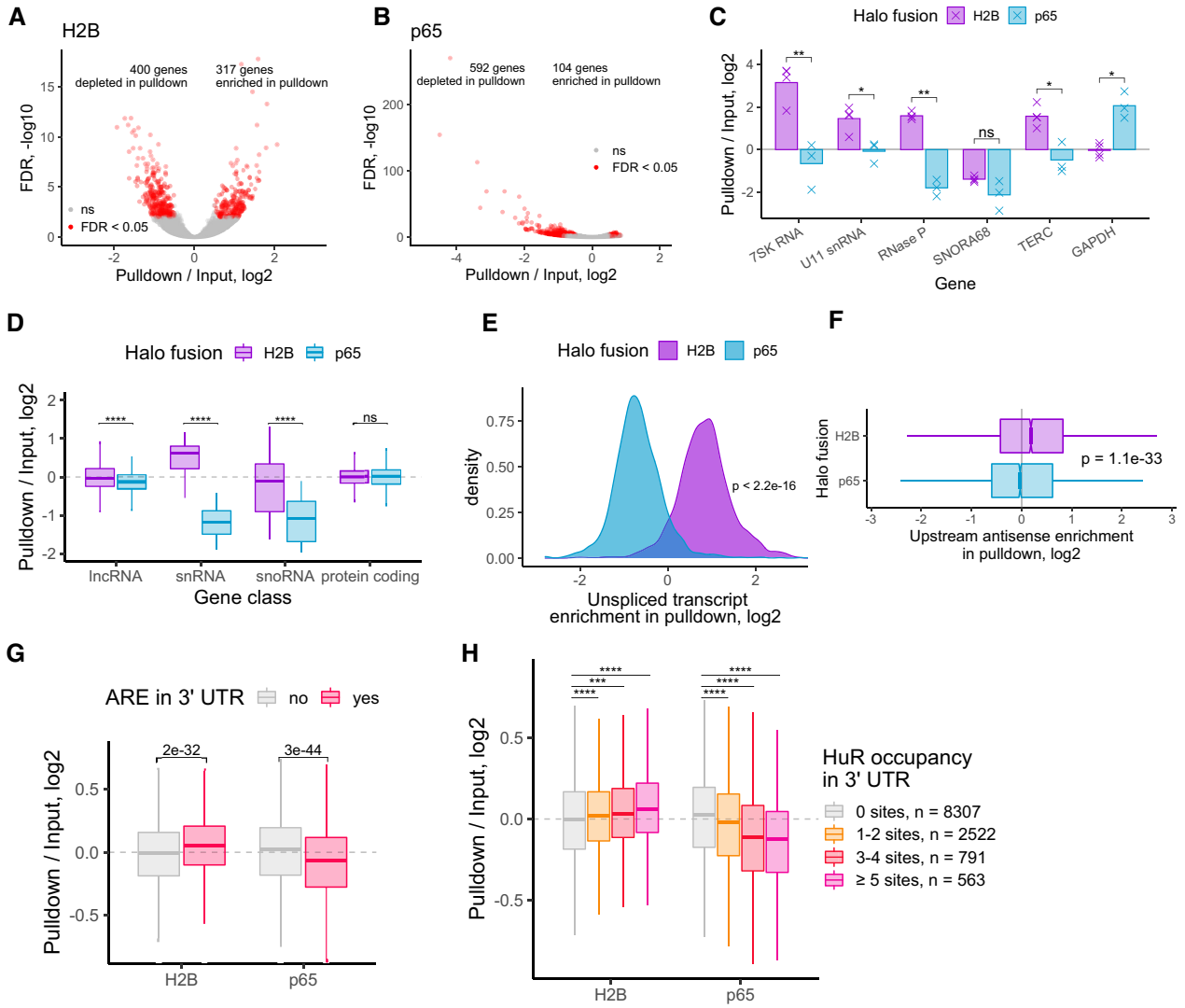

Figure 2. Halo-seq quantification of nuclear and cytoplasmic transcriptomes. (**A**) Differentially expressed genes in a comparison of pulldown and input RNA samples following Halo-seq RNA labeling using a H2B-Halo fusion. (**B**) As in A, but using a Halo-p65 fusion. (**C**) Halo-seq enrichments for selected RNA species known to be localized to the nucleus or cytoplasm. (**D**) Halo-seq enrichments for defined classes of RNAs. (**E**) Halo-seq enrichments for unspliced, intron-containing transcripts. The ratio of the abundance of unspliced transcripts to spliced transcripts was calculated for each gene. These ratios were then compared in input and pulldown samples. (**F**) Halo-seq enrichments for promoter-proximal upstream antisense transcripts. The ratio of the abundance of promoter-proximal upstream antisense to downstream transcripts was calculated for each gene. This ratio was then compared in input and pulldown samples. (**G**) Genes were binned by whether or not their 3′ UTR contained an AU-rich element (ARE). Gene enrichments in Halo-seq pulldown and input samples were then compared. (**H**) Genes were binned by the number of HuR binding sites (as defined by CLIP-seq) in their 3′ UTRs. Gene enrichments in Halo-seq pulldown and input samples were then compared. All significance tests were performed using a Wilcoxon rank-sum test. *P* value notation: * < 0.05, ** < 0.01, *** < 0.001, **** < 0.0001.

RNA in each sample using a custom Salmon index that contained both spliced and unspliced species. We then compared the ratio of unspliced to spliced abundances in the input and pulldown samples. For the H2B samples, we found that unspliced transcripts were relatively enriched in the pulldown compared to the input, whereas for the p65 samples, unspliced transcripts were depleted in the pulldown (Figure 2E, Supplementary Figure S1E, F), demonstrating that Halo-seq is able to interrogate the localization of dynamically processed RNAs.

Next, we asked whether Halo-seq could quantify intrinsically unstable and short-lived RNAs. During transcription initiation, antisense RNAs are produced from the region upstream of the promoter (38). These upstream antisense transcripts are highly unstable and very unlikely to leave the nucleus. We reasoned therefore that they should be enriched in the H2B pulldown relative to the p65 pulldown. For each gene, we calculated the ratio of upstream antisense RNAs to downstream sense RNAs. We then compared this ratio in input and pulldown samples. We found that upstream antisense RNAs were significantly more enriched in the H2B pulldown than the p65 pulldown (Figure 2F), indicating that Halo-seq can quantify highly unstable RNAs with spatial precision.

HuR-bound transcripts are enriched in the nucleus and depleted in the cytoplasm

Given the assurance in the quality of our spatially resolved nuclear and cytoplasmic transcriptomes, we searched for RNA features that discriminated between nucleus- and cytoplasm-enriched transcripts. Interestingly, we found that genes that contained AU-rich elements (AREs) in their 3′ UTRs were enriched in the H2B pulldown and depleted from the p65 pulldown (Figure 2G). AREs are RNA sequence motifs, often located in 3′ UTRs, that are most often thought to regulate transcript stability but have also been noted to regulate RNA export (39,40). HuR is an RNA-binding protein known to bind AREs (41). Accordingly, we found a dose-dependent relationship between the number of CLIP-defined HuR binding sites (42) in a gene's 3′ UTR and the degree of its enrichment in the H2B pulldown. Conversely, we found an inverted dose-dependent relationship between 3′ UTR HuR binding sites and its depletion in the p65 pulldown (Figure 2H). These results suggest that specific RNA sequences and RBPs can modulate the relative nuclear and cytoplasmic abundances of a transcript (43).

Halo-seq distinguishes transcriptomes of compartments in close proximity to each other

Although the results from our analysis of nuclear and cytoplasmic transcriptomes were highly encouraging, these two cell compartments are separated by a well-defined membrane and therefore may not provide the best scenario with which to test the spatial specificity of Halo-seq. We reasoned instead that a more rigorous test of the technique would be to differentiate the RNA contents of non-membrane-bound organelles. We therefore chose to interrogate another subcellular compartment, the nucleolus.

We began by fusing a HaloTag to a specific marker of nucleoli, Fibrillarin (44). This fusion was specifically localized to nucleoli and was distinguishable from the chromatin-associated H2B-Halo fusion using fluorescence imaging (Figure 3A). We performed the Halo-seq alkynylation and biotinylation procedures and detected biotinylated RNA from Halo-Fibrillarin-expressing cells that was dependent upon the addition of DBF, indicating that nucleolar RNA was being labeled by Halo-seq (Figure 3B). We then sequenced the transcripts enriched by Halo-Fibrillarin using libraries created with rRNA depletion. Gene expression values of streptavidin input and pulldown samples were well separated by PCA, suggesting that the Fibrillarin-mediated labeling occurred on specific transcripts (Supplementary Figure S2A). Halo-Fibrillarin labeled RNA was enriched for 602 genes and depleted for 338 genes (FDR < 0.05, absolute $\log_2$ fold change ≥ 0.5), indicating that the nucleolus contains an RNA population distinct from bulk cellular RNA (Figure 3C, Supplementary Table S3). When comparing the H2B and Fibrillarin pulldowns, only 20 genes were significantly enriched in both datasets. This overlap was not statistically significant ($P = 0.2$, binomial test) and suggests that the RNA populations labeled by Halo-seq in the two compartments were largely distinct.

As with the H2B and p65 experiments, we looked at the enrichment of RNA species previously known to be present in nucleoli (Figure 3D). Encouragingly, we found that *7SL* RNA was enriched in the Fibrillarin pulldown. This RNA is part of the signal recognition particle (SRP) ribonucleoprotein complex. SRP is involved in protein targeting to the endoplasmic reticulum in the cytoplasm, but it is assembled in the nucleolus (45). Similarly, we found that the snoRNA *SNORA68* was enriched in the Fibrillarin pulldown but not in either the nuclear or the cytoplasmic experiments. This is an encouraging result since snoRNAs are known to be primarily localized to the nucleolus (33). Importantly, both of these RNAs were depleted from the H2B pulldown, indicating that Halo-seq can distinguish the chromatin-proximal and nucleolar transcriptomes even though these two compartments are in close proximity to each other. Conversely, the transcription-regulating *7SK* RNA and the telomere-regulating *TERC* RNA were enriched in the H2B pulldown and depleted in the Fibrillarin pulldown, further highlighting the spatial specificity of Halo-seq.

To generalize these results, we calculated the enrichments of classes of RNAs (Figure 3E). snRNAs were depleted from the cytoplasmic p65 pulldown but were similarly enriched in the H2B and Fibrillarin pulldowns. Although snRNAs are mainly thought of in the context of chromatin-associated pre-mRNA splicing, they do transiently pass through the nucleolus and are modified there (46,47). snoRNAs as a class were significantly more enriched in the Fibrillarin pulldown than the H2B pulldown, again highlighting the spatial specificity of Halo-seq. Unspliced pre-mRNAs were significantly less enriched in the fibrillarin pulldown than the H2B pulldown (Figure 3F), further highlighting the specificity.

A gene ontology analysis of RNAs enriched in the Fibrillarin pulldown revealed many terms associated with ribosome biogenesis (Figure 3G). Interestingly, for both the p65 and Fibrillarin pulldowns, we observed that many RNAs derived from the mitochondrial chromosome were enriched in the pulldown (Supplementary Figure S2B). Since we do not expect these RNAs to be colocalized with the p65 or Fibrillarin Halo fusion proteins, this suggests that technical reasons may be behind their enrichment. During the Halo-seq procedure, oxygen radicals oxidize nearby ribonucleoside bases, making them targets for alkynylation through propargylamine. It may be that RNA molecules in the mitochondria are consistently subjected to similar oxidation through the reactive oxygen species naturally produced by mitochondria making them similar targets for alkynylation. Care must be taken, then, in interpreting enrichments of mitochondrial RNAs when comparing Halo-seq input and streptavidin-pulldown samples.

Comparison of Halo-seq to other high-throughput methods for studying RNA localization

Other methods for the purification and analysis of subcellular transcriptomes have been previously reported (16,18,19,48). We therefore set out to compare the sensitivity and specificity of Halo-seq to these methods.

Halo-seq utilizes a dibromofluorescein (DBF) Halo ligand; however, this ligand is not commercially available. We therefore tested the ability of this ligand to induce RNA labeling in comparison to the more commonly used and commercially available fluorescein Halo ligand. RNA bi-

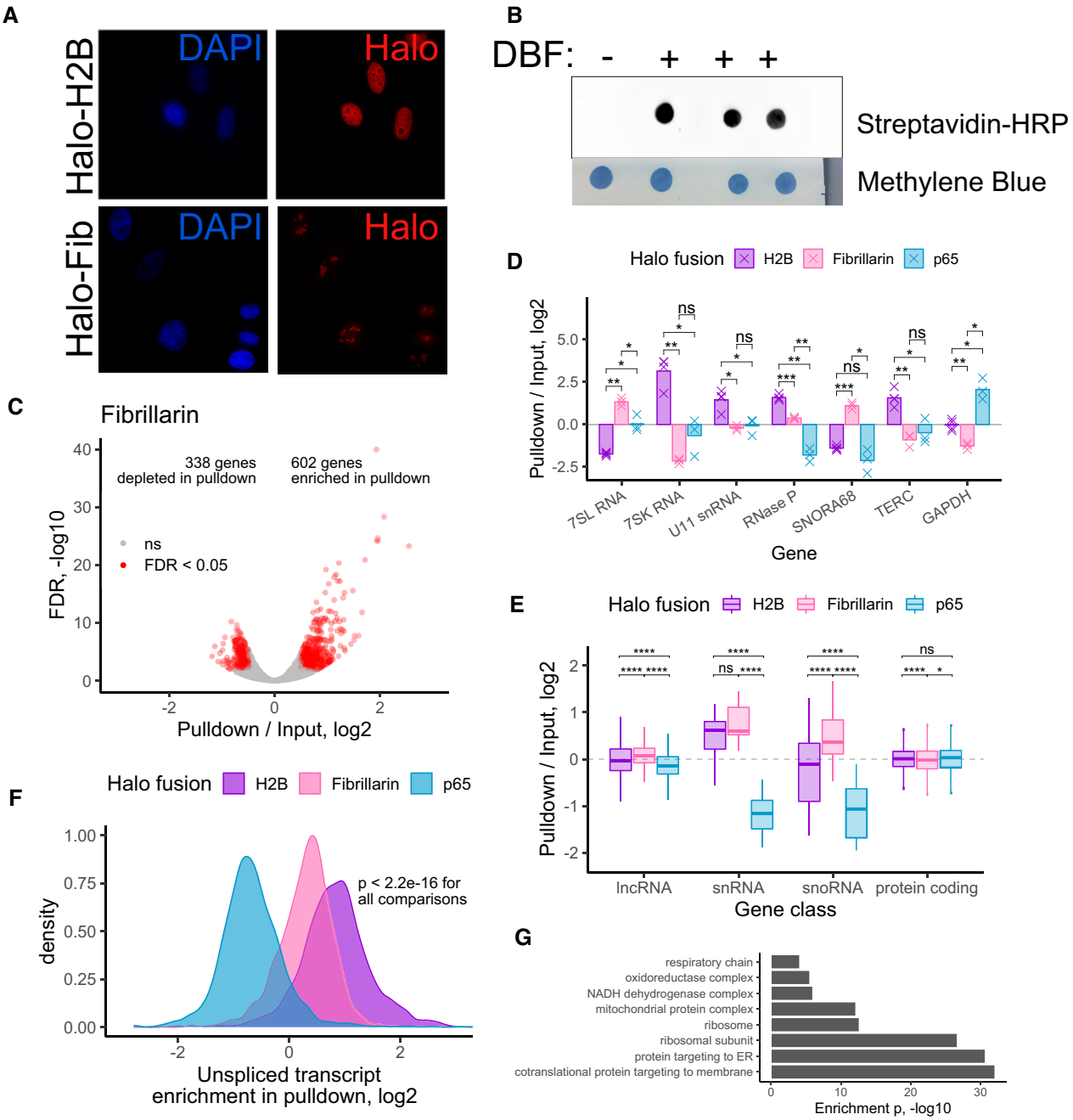

Figure 3. Halo-seq quantification of the nucleolar transcriptome. (**A**) Visualization of the subcellular location of histone H2B and fibrillarin Halo domain fusions. Halo fusion proteins were visualized using a fluorescent Halo ligand. (**B**) RNA dot blot of RNA collected from cells expressing a Halo-fibrillarin fusion protein. (**C**) Differentially expressed genes in a comparison of pulldown and input RNA samples following Halo-seq RNA labeling using a Halo-fibrillarin fusion. (**D**) Halo-seq enrichments for selected RNA species known to be localized to the nucleus, nucleolus, or cytoplasm. (**E**) Halo-seq enrichments for defined classes of RNAs. (**F**) Halo-seq enrichments for unspliced, intron-containing transcripts. As in Figure 2E, the ratio of the abundance of unspliced transcripts to spliced transcripts was calculated for each gene. This ratio was then compared in input and pulldown samples. (**G**) Enriched gene ontology terms derived from RNAs identified as localized to the nucleolus. All significance tests were performed using a Wilcoxon rank-sum test. *P* value notation: * < 0.05, ** < 0.01, *** < 0.001, **** < 0.0001.

otinylation was assayed using dotblots following reactions with these two ligands in HaloTag-expressing cells (Figure 4A). RNA labeling reactions with DBF produced considerably more biotinylated RNA than those with fluorescein, indicating that DBF is more efficient at facilitating RNA alkynylation than fluorescein. This is consistent with previous reports demonstrating that DBF is a more efficient singlet oxygen generator and has a much higher singlet oxygen yield ($\Phi\Delta$; 0.42) than that of fluorescein (49). Critically, the increased singlet oxygen production by DBF results in higher yield of RNA oxidation for subsequent tagging by propargylamine. This difference is explained by heavy atoms (bromine) increasing the likelihood that photoexcited chromophores will undergo an intersystem crossing (ISC) to the triplet state, from which $^1O_2$ can be generated from ground state O_2. The drastic difference in RNA tagging suggests that the choice of fluorophore and understanding its singlet oxygen yield is critical for the further development of Halo-seq.

Cap-seq, a similar method that uses the blue-light activated singlet oxygen generator miniSOG2 to label RNAs was recently reported (18). In this approach, miniSOG2 generates radicals that, together with propargylamine, can alkynylate nearby RNA molecules. To test the relative labeling efficiency of the miniSOG2- and Halo-based methods, we created a HeLa cell line that inducibly expressed a miniSOG2-Halo fusion protein from a single, defined locus (Supplementary Figure S3A). This strategy ensures that miniSOG2 and Halo are expressed at equal amounts.

We then performed RNA labeling in these cells under two conditions: either (i) without DBF and using blue light activation or (ii) with DBF and using green light activation. Under the first condition, we would expect any labeling to be due to the activity of miniSOG2. Because miniSOG2 is activated only by light, it is possible that miniSOG2-mediated labeling could also happen in the second condition. However, because Halo-mediated labeling requires DBF, the *difference* in labeling between the conditions is likely attributable to Halo-mediated labeling.

We observed very little RNA labeling using blue light activation in the absence of DBF. In contrast, we observed robust RNA labeling upon the addition of DBF and green light (Figure 4B). We therefore conclude that DBF is a more efficient RNA labeller than miniSOG2.

One explanation for the striking difference between the two is the singlet oxygen yield, which is related to the stability of both the chromophore and its excited state. The singlet oxygen yield of DBF is 0.42 while that of miniSOG is 0.03 (50). It is also well established with miniSOG that the formation of radicals (and singlet oxygen) results in protein damage near the chromophore, which limits the generation of more radicals over time. Prolonged irradiation to blue light leads to several structural alterations of miniSOG (51), which include photodegradation of FMN and oxidation of the quenching side chains. These results are expected to be a general feature of flavin-binding proteins (52).

Another RNA proximity labeling technique that utilizes radical generation is APEX-seq (16,19). Similarly to Halo-seq, APEX-seq relies on a spatially restricted fusion protein to facilitate spatially restricted RNA labeling. In APEX-seq, a spatially restricted protein is fused to the radical-generating enzyme APEX2. We compared the efficiency of DBF-mediated and APEX2-mediated RNA labeling by creating a cell line that expressed a Halo-APEX2 fusion protein. As with the miniSOG2 experiments, this strategy ensures that the HaloTag domain and APEX2 enzyme are expressed at equal amounts (Supplementary Figure S3B). Using these cells, we then performed RNA labeling using the Halo-seq or APEX-seq methods (16,19). With both methods, we observed more labeling in the experimental samples than their respective controls (DBF omission for Halo-seq, hydrogen peroxide omission for APEX-seq). However, we observed approximately 10-fold more labeling in the Halo-seq experimental sample than the APEX-seq experimental sample, suggesting that DBF-mediated RNA labeling is more efficient than APEX2-mediated RNA labeling (Figure 4C). Differences in RNA labeling efficiency may be due to the short-lived nature of the APEX-derived radicals and their known propensity to cleave RNA, which would reduce the reactive capacity of generated tyramide radicals for tagging.

To further compare Halo-seq and APEX-seq, we compared RNA enrichments (pulldown / input) in cytoplasmic, nuclear, and nucleolar samples using hierarchical clustering (Supplementary Figure S3C). Unfortunately, APEX-seq RNAseq libraries were produced using polyA-enrichment, precluding quantification of the small RNA species (e.g. snRNAs and snoRNAs) that can serve as specific markers of these subcellular fractions. Nevertheless, we found that cytoplasmic samples from Halo-seq and APEX-seq clustered together, indicating their similarity. Nuclear samples from the two methods also clustered together. Conversely, the nucleolar samples from the two methods did not cluster together. Nucleolar samples from APEX-seq were similar to the nuclear samples from both methods while the nucleolar samples from Halo-seq were well separated from all other samples. In addition to differences in library preparation techniques, the use of different proteins as nucleolar markers may also play a role as we used Fibrillarin while NIK was used in the APEX-seq experiments. Given that the nucleolus is dissolved during mitosis (53), these markers may have different subcellular distributions in mitotic cells, further contributing to observed differences in the nucleolar Halo-seq and APEX-seq data.

Other methods to study RNA localization rely on biochemical fractionation rather than proximity labeling (48). One such study used CeFra-seq to biochemically separate two cultured cell lines, HepG2 and K562, into nuclear, cytosolic, insoluble, and membrane-associated fractions. RNAseq libraries prepared from these fractions were constructed using rRNA-depletion, allowing direct comparison of these results with Halo-seq. We first used hierarchical clustering to compare gene enrichment values (pulldown/input for Halo-seq, fraction/total for CeFra-seq) produced by the two methods (Supplementary Figure S3D). While the nuclear samples of the two methods were well correlated, the cytoplasmic CeFra-seq samples were more related to the nucleolar Halo-seq samples than the cytoplasmic Halo-seq samples.

We then compared gene enrichments from specific gene classes. Whereas both methods showed enrichments for snRNAs in their nuclear fraction, CeFra-seq showed en-

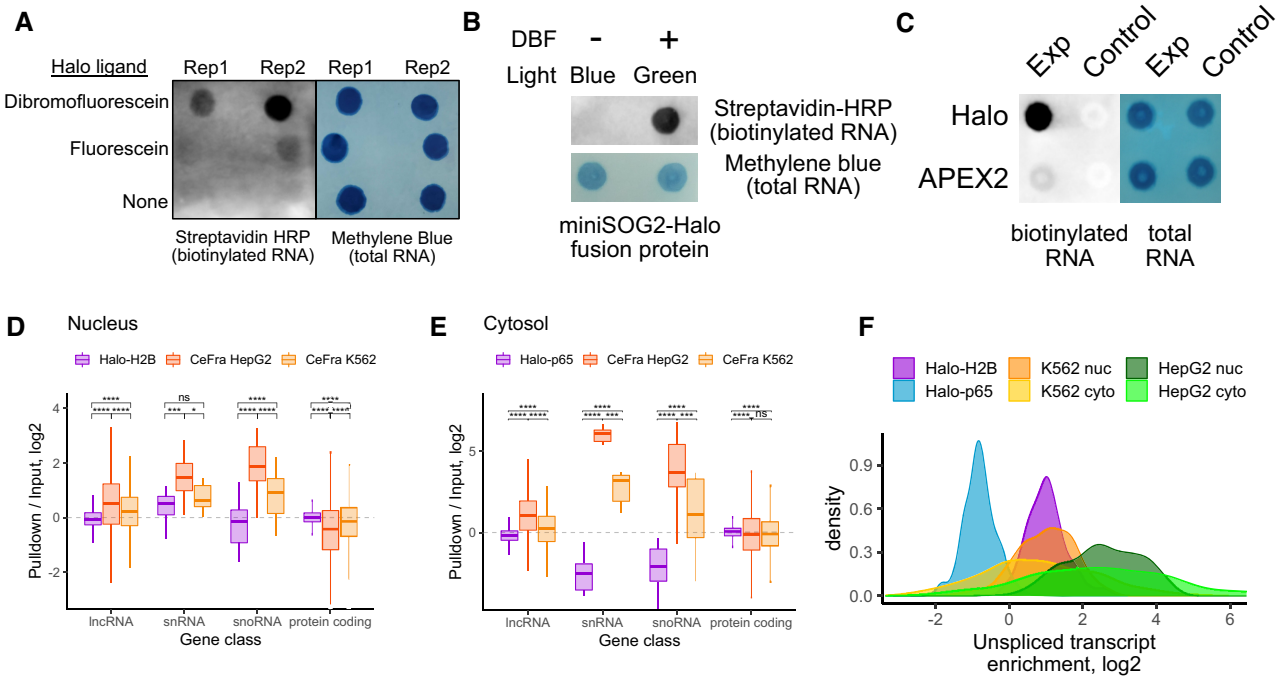

Figure 4. Comparison of Halo-seq with similar methods for quantifying RNA localization transcriptome-wide. (**A**) RNA biotinylation, as assayed by RNA dot blot, in cells expressing a HaloTag domain and treated with Halo ligand forms of dibromofluorescein (DBF) or fluorescein. (**B**) Comparison of RNA biotinylation efficiency of Halo-seq and CAP-seq, a similar RNA proximity labeling method that uses miniSOG2, an enzymatic singlet oxygen generator. For the Halo-expressing cells, the experimental and control conditions correspond to the addition or omission of DBF, respectively. For the miniSOG2-expressing cells, the experimental and control conditions correspond to the treatment or omission of blue light irradiation. (**C**) Comparison of RNA biotinylation efficiency of Halo-seq and APEX-seq. For the Halo-expressing cells, the experimental and control conditions correspond to the addition or omission of DBF, respectively. For the APEX2-expressing cells, the experimental and control conditions correspond to the inclusion or omission of hydrogen peroxide. (**D**) Comparison of nuclear enrichments for selected gene classes using data produced by Halo-seq and CeFra-seq. The Halo-seq data corresponds to enrichments from the H2B-Halo-mediated labeling experiment described previously. The CeFra-seq data corresponds to enrichments in a biochemically defined nuclear fraction compared to total RNA from an unfractionated sample. (**E**) As in D, comparison of cytosolic enrichments for selected gene classes. The Halo-seq data corresponds to enrichments from the Halo-p65-mediated labeling experiment described earlier. The CeFra-seq data corresponds to enrichments in a biochemically defined cytosolic fraction compared to total RNA from an unfractionated sample. (**F**) Enrichments for unspliced, intron-containing transcripts. The ratio of the abundance of unspliced transcripts to spliced transcripts was calculated for each gene. For Halo-seq samples, this ratio was then compared in input and pulldown samples. For CeFra-seq samples, this ratio was then compared in fractionated (either nuclear or cytosolic) and total, unfractionated samples. All significance tests were performed using a Wilcoxon rank-sum test. *P* value notation: * < 0.05, ** < 0.01, *** < 0.001, **** < 0.0001.

richments for snoRNAs in the nuclear fraction while Halo-seq did not (Figure 4D). This is likely due to the inability of CeFra-seq to distinguish between the nucleus and nucleolus. Interestingly, in the cytoplasmic CeFra-seq samples, snRNAs and snoRNAs were enriched, even though these are nuclear and nucleolar markers, respectively (Figure 4E). Similarly, unspliced transcripts were comparably enriched in the nuclear and cytoplasmic CeFra-seq samples even though unspliced transcripts are generally found in the nucleus (Figure 4F). From these findings, we conclude that Halo-seq is better suited to isolating subcellular transcriptomes than the biochemical CeFra-seq method. Further, the flexibility of Halo-seq allows the interrogation of subcellular compartments that are not amenable to biochemical purification.

Halo-seq identifies RNA targets of the CRM1-dependent RNA export pathway

Given that we had established that Halo-seq allows the efficient and accurate profiling of subcellular transcriptomes, we moved to the quantification of RNA localization following perturbation. A subset of transcripts in mammalian cells depend upon the action of CRM1 for export from the nucleus, and the small molecule leptomycin B (LMB) inhibits the action of CRM1 (54). While the identity of a handful of RNAs that are nuclearly retained following LMB treatment are known (55,56), the full complement of RNAs that depend on CRM1 for export remains unknown.

To more fully investigate the dependence on CRM1 for RNA export, we identified nuclearly enriched RNAs using Halo-seq with a H2B-Halo fusion in the presence and absence of LMB. Following LMB treatment, we expected an increased nuclear abundance for a subset of RNAs whose nuclear export depends on CRM1.

We first verified that the nuclear localization of the H2B-Halo fusion protein did not change following LMB treatment (Figure 5A). Our cytoplasmic Halo-p65 marker contained a CRM1-dependent nuclear export motif and was correspondingly restricted to the nucleus following LMB treatment (Figure 5A). While this excluded it from being a useful cytoplasmic marker in this experiment, it provided

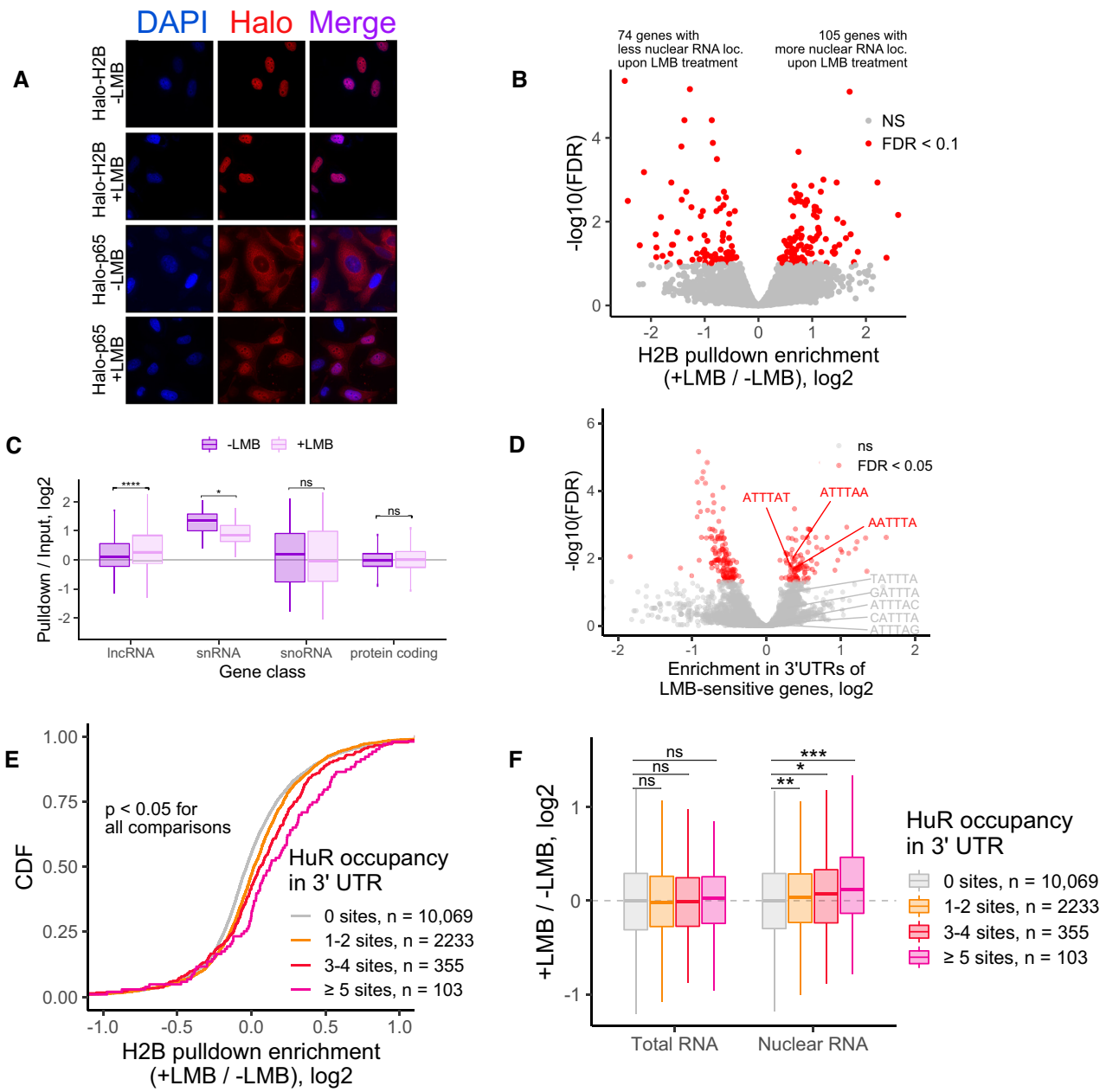

Figure 5. Halo-seq identifies transcriptome-wide changes in RNA localization following treatment with leptomycin B. (**A**) Visualization of the subcellular localization of Halo fusion proteins using a fluorescent Halo ligand. Note that while the p65 fusion is normally cytoplasmic, upon treatment with LMB, it becomes nuclear, indicating inhibition of CRM1 mediated export upon LMB treatment. (**B**) Volcano plot depicting changes in Halo-seq H2B pulldown enrichment (i.e. nuclear localization) following LMB treatment. (**C**) Changes in H2B pulldown enrichment following LMB treatment for selected gene classes. (**D**). Kmers of length 6 enriched in the 3′ UTRs of genes whose H2B pulldown enrichment was sensitive to LMB compared to the 3′ UTRs of genes whose H2B pulldown enrichment was not sensitive to LMB. (**E**) Genes were binned by the number of HuR binding sites (as defined by CLIP-seq) in their 3′ UTRs. Enrichments in H2B pulldown samples from LMB treated and untreated samples were then compared. (**F**) Abundance changes in total RNA (left) and nuclear RNA (right) following LMB treatment as a function of the number of HuR binding sites in the 3′ UTRs of transcripts. Total RNA and nuclear RNA samples correspond to the input and pulldown samples from H2B-targeted Halo-seq experiments. All significance tests were performed using a Wilcoxon rank-sum test. *P* value notation: * < 0.05, ** < 0.01, *** < 0.001, **** < 0.0001.

clear validation that the LMB treatment inhibited CRM1 activity under these conditions.

LMB treated and untreated samples displayed approximately the same amount of labeled nuclear RNA as assayed by streptavidin-HRP RNA dotblot (Supplementary Figure S4A). RNAseq analysis of the treated and untreated samples revealed that the RNA of 105 genes was significantly more enriched in the H2B pulldown sample in the LMB treated sample than the LMB untreated sample (FDR < 0.1) (Figure 5B, Supplementary Figure S4B, Table S4).

We then asked about the relative nuclear enrichment of different RNA classes (Figure 5C). As a class, lncRNAs were more nuclearly enriched following LMB treatment, suggesting that they may broadly depend on CRM1 for export. The nuclear enrichment of snRNAs was decreased following LMB treatment, in line with reports documenting that CRM1 is required for snRNP maturation and retention in nuclear Cajal bodies (57). The nuclear enrichment of snoRNAs and protein-coding mRNAs were unaffected.

We defined transcripts whose nuclear export was sensitive to LMB (FDR < 0.05) using the software package Xtail (58). To identify transcript features associated with LMB sensitivity, we used a software package we created called FeatureReachR (https://github.com/TaliaferroLab/FeatureReachR). Using FeatureReachR, we found that the 3′ UTRs of transcripts whose localization was LMB-sensitive were enriched for several AU-rich kmers (Figure 5D, Supplementary Figure S4C).

Given the enrichment observed in LMB-sensitive transcripts for AU-rich kmers and motifs, we then directly searched these transcripts for AREs using a previously compiled database of their locations (59). We found that LMB-sensitive transcripts were enriched for AREs in their 3′ UTRs (Supplementary Figure S4D).

AREs can be bound by several different RBPs, including HuR (also known as ELAVL1) (60). HuR has previously been identified as a protein whose export to the cytoplasm depends on CRM1 (61). Using FeatureReachR's ability to search for enrichment of the known binding motifs of many RBPs, we found that HuR RNA motifs were enriched in the 3′ UTRs of LMB-sensitive transcripts (Supplementary Figure S4E). To extend this analysis to HuR binding sites identified in cells, we used HuR CLIP-seq data. The number of HuR binding sites in the 3′ UTRs of LMB-sensitive transcripts showed a dose-dependent relationship with the amount of increased nuclear enrichment of the transcript following LMB treatment (Figure 5E).

Since Halo-seq enrichments are calculated as a ratio of abundances in streptavidin-pulldown and input RNA, the increased enrichment of HuR-bound RNAs following LMB treatment could be due to either an increase in the abundance of HuR targets in the H2B pulldown or a decrease in their abundance in input samples. To distinguish between these possibilities, we compared LMB-induced abundance changes in the input and H2B pulldown samples separately. We found that the abundance of HuR target RNAs in total RNA (input) samples did not change upon LMB treatment. In contrast, the abundance of HuR target RNAs in the nuclear (pulldown) samples significantly increased upon LMB treatment (Figure 5F). These results suggest that hundreds of RNAs depend on HuR for efficient export from the nucleus.

DISCUSSION

In this study, we have developed an RNA proximity method called Halo-seq that has the capability to isolate and quantify subcellular transcriptomes. We used Halo-seq to analyze nuclear and cytoplasmic transcriptomes and found that ARE-containing transcripts are relatively enriched in the nucleus and depleted from the cytoplasm. The capacity of AREs to negatively regulate RNA stability has been extensively established (42,62), but their ability to induce differential nucleocytoplasmic localization at steady state has not been reported. One of the key RBPs that binds AREs to induce RNA degradation, Tristetraprolin, is predominantly localized to the cytoplasm (63). One possible explanation, then, of the observed nuclear enrichment and cytoplasmic depletion of ARE-containing transcripts is that these RNAs are more vulnerable to degradation in the cytoplasm than in the nucleus (Figure 6A).

We then assayed dynamic RNA localization in response to treatment with the nuclear export inhibitor LMB. We found a dose-dependent relationship between the number of 3′ UTR HuR binding sites an RNA contained and the degree to which its abundance in the nucleus was increased following LMB treatment. HuR is known to both increase the stability of the RNAs that it binds (42) and be important for the nuclear export of at least a handful of RNAs (61). Although HuR shuttles between the nucleus and cytoplasm, its export from the nucleus is inhibited by LMB (61). We therefore propose two non-exclusive models to explain the observed increase in nuclear abundance of HuR bound RNAs following LMB treatment (Figure 6B).

In one scenario, LMB-induced retention of HuR in the nucleus increases the vulnerability of its target RNAs to cytoplasmic degradation as its ability to protect its targets from instability has been lost. In an alternative scenario, RNAs that depend on HuR for nuclear export are now less efficiently exported, leading to their accumulation in the nucleus.

Nuclear RNA makes up a relative minority of total cellular RNA while cytoplasmic RNA makes up the majority. If the primary effect of LMB treatment on HuR-bound transcripts was a loss of stability, particularly in the cytoplasm, then we would expect to find that their levels in total RNA would be decreased. However, if the loss of HuR-mediated export was heavily involved, then we would expect to see HuR-bound RNAs become more abundant in the nucleus. Since, though, nuclear RNA makes up a small fraction of total RNA, their overall abundance may be unchanged. Importantly, we found that the overall levels of HuR-bound transcripts were unchanged following LMB treatment while their levels in the nucleus significantly increased (Figure 5F). These results are consistent with the idea that HuR regulates the nuclear export of hundreds of transcripts.

We believe these results are important in the context of the existing literature describing HuR activity. Although HuR has been previously found to regulate the nuclear export of a limited number of RNAs (61), the vast majority

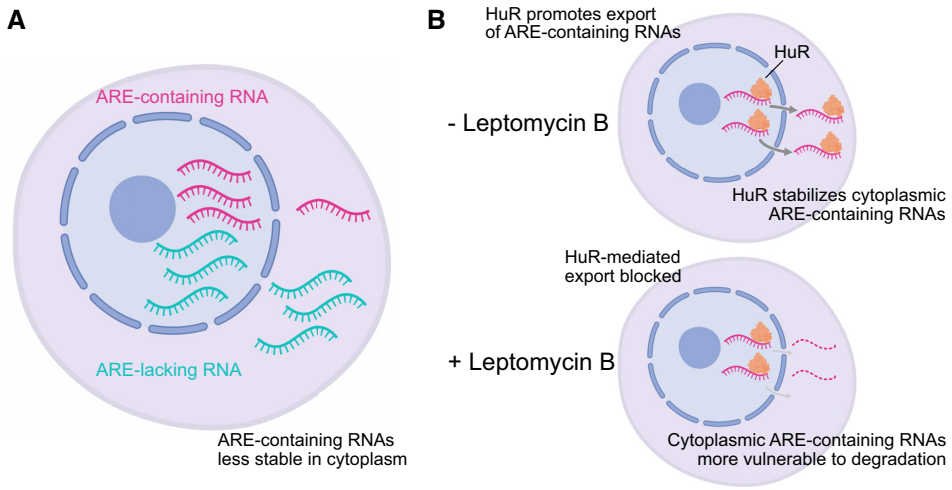

Figure 6. Model for observed differences in nuclear and cytoplasmic transcript abundances. (**A**) ARE-containing RNAs were relatively less abundant in the cytoplasm than the nucleus in our Halo-seq experiments. Cytoplasmic localization of many proteins that drive ARE-mediated RNA degradation, including TTP, could be a major contributing factor to this observation. (**B**) Upon LMB treatment, ARE-containing RNAs become even more relatively enriched in the nucleus. AREs are often bound by HuR, which both participates in RNA export and stabilizes cytoplasmic ARE-containing transcripts. HuR export from the nucleus is blocked by LMB, resulting in decreased export of ARE-containing transcripts and/or their increased vulnerability to degradation in the cytoplasm.

of the work on HuR has focused on its capacity to regulate RNA stability. These results therefore simultaneously greatly expand our knowledge of the transcripts that use HuR for nuclear export and provide strong confidence that Halo-seq can accurately quantify dynamic subcellular localization and be used to derive mechanistic insights regarding its regulation.

Using known markers of nuclear and nucleolar RNA, we found that Halo-seq can efficiently distinguish the RNA contents of these two compartments. Given their close spatial proximity, these results favorably report on the ability of Halo-seq to quantify RNA localization with high spatial precision.

Interestingly, we found a consistent enrichment of RNAs derived from the mitochondrial chromosome in Halo-seq pulldown samples compared to input samples. This was most prevalent in the p65 and Fibrillarin Halo-seq experiments (Supplementary Figure S2B). We believe that given the observed cellular distributions of the Halo fusion proteins, it is unlikely that this enrichment reflects Halo-induced RNA labeling. We therefore propose an alternate explanation. During the Halo-seq labeling process, DBF-proximal ribonucleotides are oxidized by singlet oxygen radicals, making them targets for alkynylation through nucleophilic attack by propargylamine. Mitochondrial transcripts may be similarly oxidized by reactive oxygen species naturally produced by mitochondrial function. They may therefore be similar, yet DBF-independent, targets for alkynylation. We believe that caution should be used when interpreting enrichments of mitochondrial transcripts when comparing Halo-seq input and pulldown samples. This issue may be mitigated somewhat if instead two Halo-seq pulldown samples were compared (e.g. one from a Halo fusion that was specifically localized to a region of interest and another that was broadly, non-specifically localized). In this case, any putative mitochondrial-dependent alkynylation would be present in both samples and its effect therefore minimized.

The ability of Halo-seq to recapitulate known RNA localization patterns as well as its ability to connect these patterns to activities of specific RBPs gave us confidence that the method performed well. However, a number of approaches for quantifying subcellular transcriptomes had been previously reported (16–19,48). We therefore compared the efficiency and specificity of RNA labeling produced by Halo-seq to these methods.

CeFra-seq uses biochemical fractionation to define subcellular fractions (48). Although we observed some agreement between the nuclear and cytoplasmic RNA contents defined by CeFra-seq, we found that Halo-seq performed better in terms of correctly placing RNAs of known localization. A key advantage of proximity labeling schemes, including Halo-seq, over biochemical fractionations is that the important labeling steps are performed while cells are alive and intact. Biochemical fractionations are inherently susceptible to false positives in which RNAs that are spatially distinct within a cell yet possess similar biochemical properties copurify. They are also susceptible to false negatives in which the association of spatially coincident RNAs does not survive the biochemical purification. These factors may explain the superior performance of Halo-seq.

Two RNA proximity labeling techniques, APEX-seq and CAP-seq, were also recently reported (16,18,19). We observed a general agreement in the quantification of localized RNAs with Halo-seq and APEX-seq, although we were unable to quantify the localization of small RNAs in the APEX-seq data due to their use of oligo-dT enrichment instead of rRNA depletion. We were unable to directly compare RNA localization patterns observed by Halo-seq to those observed by CAP-seq due to the fact that the raw sequencing data from the report describing CAP-seq has not to our knowledge been made publicly available.

We compared RNA labeling efficiencies of all three proximity labeling methods (Figure 4B, C). We found that Halo-seq was significantly more efficient in generating labeled RNA than both APEX-seq and CAP-seq. These observations may be attributed to differences in the efficiency of miniSOG-dependent singlet oxygen generation or the reactive species that is being generated by APEX-seq in comparison to the singlet oxygen from DBF excitation. The increased efficiency of Halo-seq may make it better suited to the study of precisely defined subcellular RNA populations that make up a relatively small proportion of the total cellular RNA content. Halo-seq may therefore allow interrogation of the RNA content of small, defined locations that until now were intractable for such experiments.

Although we believe Halo-seq has considerable promise, a number of potential hurdles remain. Halo-seq requires the use of Halo-tagged fusion proteins. The subcellular localization of fusion proteins is often hard to predict and must be empirically verified. The use of transgenes for fusion protein expression is experimentally simple, but the overexpression that occurs with these constructs can often lead to spurious, unintended localization patterns. Tagging endogenous genes with Halo domains may alleviate this problem.

Additionally, as with most methods, a certain level of background exists with Halo-seq. This manifests as transcripts that are precipitated by the streptavidin pulldown even though they were not alkynylated in the cell. When querying large subcellular regions when a considerable amount of RNA is expected to be labeled, this level of background is likely overcome by true signal. However, when querying small, specific locations, the background signal may pose serious issues. One potential approach to minimize this effect may be to compare two pulldown samples where one originates from a sample with a Halo fusion localized to the location of interest and another originates from a sample with a broadly localized Halo fusion (e.g. Halo-NES).

One interesting application of this technique may be to the projections of neuronal cells. RNA localization in neurons has been extensively studied on a transcriptome-wide scale (4,13,14,64,65). However, generally, these studies have relied on rather coarse-grained fractionations that lack the resolution required to make statements about RNA localization to specific structures (e.g. synapses). The increased resolution of Halo-seq may allow for deeper insights regarding the organization of RNA within neuronal projections.

In sum, we view Halo-seq as a flexible, quantitative tool that is well-suited to advance the study of subcellular RNA localization.

DATA AVAILABILITY

All high-throughput RNA sequencing data as well as transcript quantifications have been deposited at the Gene Expression Omnibus under accession number GSE172281.

SUPPLEMENTARY DATA

Supplementary Data are available at NAR Online.

ACKNOWLEDGEMENTS

We thank members of the Taliaferro lab for helpful discussions regarding experiments and analyses. We also thank Neel Mukherjee for helpful discussion and tips regarding analysis of Halo-seq data. Portions of the figures in this manuscript were created using BioRender.

FUNDING

National Institutes of Health [R35-GM133885 to J.M.T., DP2 GM119164 to R.C.S.]; W.M. Keck Foundation (to J.M.T.); RNA Bioscience Initiative at the University of Colorado Anschutz Medical Campus (to J.M.T., H.Y.L., R.G.); Predoctoral Training Grant in Molecular Biology [NIH-T32-GM008730 to H.Y.G.L., R.G.). Funding for open access charge: NIH [R35-GM133885].

Conflict of interest statement. None declared.

REFERENCES

1. Long,R.M., Singer,R.H., Meng,X., Gonzalez,I., Nasmyth,K. and Jansen,R.P. (1997) Mating type switching in yeast controlled by asymmetric localization of ASH1 mRNA. *Science*, **277**, 383–387.
2. Lécuyer,E., Yoshida,H., Parthasarathy,N., Alm,C., Babak,T., Cerovina,T., Hughes,T.R., Tomancak,P. and Krause,H.M. (2007) Global analysis of mRNA localization reveals a prominent role in organizing cellular architecture and function. *Cell*, **131**, 174–187.
3. Moor,A.E., Golan,M., Massasa,E.E., Lemze,D., Weizman,T., Shenhav,R., Baydatch,S., Mizrahi,O., Winkler,R., Golani,O. *et al.* (2017) Global mRNA polarization regulates translation efficiency in the intestinal epithelium. *Science*, **357**, 1299–1303.
4. Cajigas,I.J., Tushev,G., Will,T.J., tom Dieck,S., Fuerst,N. and Schuman,E.M. (2012) The local transcriptome in the synaptic neuropil revealed by deep sequencing and high-resolution imaging. *Neuron*, **74**, 453–466.
5. Ephrussi,A. and Lehmann,R. (1992) Induction of germ cell formation by oskar. *Nature*, **358**, 387–392.
6. Ghosh,S., Marchand,V., Gáspár,I. and Ephrussi,A. (2012) Control of RNP motility and localization by a splicing-dependent structure in oskar mRNA. *Nature Publishing Group*, **19**, 441–449.
7. Martin,K.C. and Ephrussi,A. (2009) mRNA localization: gene expression in the spatial dimension. *Cell*, **136**, 719–730.
8. Engel,K.L., Arora,A., Goering,R., Lo,H.-Y.G. and Taliaferro,J.M. (2020) Mechanisms and consequences of subcellular RNA localization across diverse cell types. *Traffic*, **21**, 404–418.
9. Taliaferro,J.M. (2019) Classical and emerging techniques to identify and quantify localized RNAs. *Wiley Interdiscip. Rev. RNA.*, **10**, e1542.
10. Chen,K.H., Boettiger,A.N., Moffitt,J.R., Wang,S. and Zhuang,X. (2015) RNA imaging. Spatially resolved, highly multiplexed RNA profiling in single cells. *Science*, **348**, aaa6090.
11. Shah,S., Lubeck,E., Zhou,W. and Cai,L. (2016) In situ transcription profiling of single cells reveals spatial organization of cells in the mouse hippocampus. *Neuron*, **92**, 342–357.
12. Gumy,L.F., Yeo,G.S.H., Tung,Y.-C.L., Zivraj,K.H., Willis,D., Coppola,G., Lam,B.Y.H., Twiss,J.L., Holt,C.E. and Fawcett,J.W. (2011) Transcriptome analysis of embryonic and adult sensory axons reveals changes in mRNA repertoire localization. *RNA*, **17**, 85–98.
13. Taliaferro,J.M., Vidaki,M., Oliveira,R., Olson,S., Zhan,L., Saxena,T., Wang,E.T., Graveley,B.R., Gertler,F.B., Swanson,M.S. *et al.* (2016) Distal alternative last exons localize mRNAs to neural projections. *Mol. Cell*, **61**, 821–833.
14. Zappulo,A., Van Den Bruck,D., Ciolli Mattioli,C., Franke,V., Imami,K., McShane,E., Moreno-Estelles,M., Calviello,L., Filipchyk,A., Peguero-Sanchez,E. *et al.* (2017) RNA localization is a key determinant of neurite-enriched proteome. *Nat. Commun.*, **8**, 583.
15. Zivraj,K.H., Tung,Y.C.L., Piper,M., Gumy,L., Fawcett,J.W., Yeo,G.S.H. and Holt,C.E. (2010) Subcellular profiling reveals distinct and developmentally regulated repertoire of growth cone mRNAs. *J. Neurosci.*, **30**, 15464–15478.

16. Fazal,F.M., Han,S., Parker,K.R., Kaewsapsak,P., Xu,J., Boettiger,A.N., Chang,H.Y. and Ting,A.Y. (2019) Atlas of subcellular RNA localization revealed by APEX-Seq. *Cell*, **178**, 473–490.
17. Kaewsapsak,P., Shechner,D.M., Mallard,W., Rinn,J.L. and Ting,A.Y. (2017) Live-cell mapping of organelle-associated RNAs via proximity biotinylation combined with protein-RNA crosslinking. *Elife*, **6**, e29224.
18. Wang,P., Tang,W., Li,Z., Zou,Z., Zhou,Y., Li,R., Xiong,T., Wang,J. and Zou,P. (2019) Mapping spatial transcriptome with light-activated proximity-dependent RNA labeling. *Nat. Chem. Biol.*, **15**, 1110–1119.
19. Padrón,A., Iwasaki,S. and Ingolia,N.T. (2019) Proximity RNA labeling by APEX-Seq reveals the organization of translation initiation complexes and repressive RNA granules. *Mol. Cell*, **75**, 875–887.
20. Li,Y., Aggarwal,M.B., Nguyen,K., Ke,K. and Spitale,R.C. (2017) Assaying RNA localization in situ with spatially-restricted nucleobase oxidation. *ACS Chem. Biol.*, **12**, 2709–2714.
21. Li,Y., Aggarwal,M.B., Ke,K., Nguyen,K. and Spitale,R.C. (2018) Improved analysis of RNA localization by spatially restricted oxidation of RNA-protein complexes. *Biochemistry*, **57**, 1577–1581.
22. Los,G.V., Encell,L.P., McDougall,M.G., Hartzell,D.D., Karassina,N., Zimprich,C., Wood,M.G., Learish,R., Ohana,R.F., Urh,M. *et al.* (2008) HaloTag: a novel protein labeling technology for cell imaging and protein analysis. *ACS Chem. Biol.*, **3**, 373–382.
23. Skovsen,E., Snyder,J.W., Lambert,J.D.C. and Ogilby,P.R. (2005) Lifetime and diffusion of singlet oxygen in a cell. *J. Phys. Chem. B*, **109**, 8570–8573.
24. Moan,J. (1990) On the diffusion length of singlet oxygen in cells and tissues. *J. Photochem. Photobiol. B*, **6**, 343–344.
25. Hein,C.D., Liu,X.M. and Wang,D. (2008) Click chemistry, a powerful tool for pharmaceutical sciences. *Pharm. Res.*, **25**, 2216–2230.
26. Khandelia,P., Yap,K. and Makeyev,E.V. (2011) Streamlined platform for short hairpin RNA interference and transgenesis in cultured mammalian cells. *Proc. Natl. Acad. Sci. U.S.A.*, **108**, 12799–12804.
27. Patro,R., Duggal,G., Love,M.I., Irizarry,R.A. and Kingsford,C. (2017) Salmon provides fast and bias-aware quantification of transcript expression. *Nat. Methods*, **14**, 417–419.
28. Soneson,C., Love,M.I. and Robinson,M.D. (2015) Differential analyses for RNA-seq: transcript-level estimates improve gene-level inferences. *F1000Res.*, **4**, 1521.
29. Love,M.I., Huber,W. and Anders,S. (2014) Moderated estimation of fold change and dispersion for RNA-seq data with DESeq2. *Genome Biol.*, **15**, 550.
30. Egloff,S., Studniarek,C. and Kiss,T. (2018) 7SK small nuclear RNA, a multifunctional transcriptional regulatory RNA with gene-specific features. *Transcription*, **9**, 95–101.
31. Altman,S. (2011) Ribonuclease P. *Philos. Trans. R. Soc. Lond. B Biol. Sci.*, **366**, 2936–2941.
32. Zhang,Q., Kim,N.-K. and Feigon,J. (2011) Architecture of human telomerase RNA. *Proc. Natl. Acad. Sci. U.S.A.*, **108**, 20325–20332.
33. Liang,J., Wen,J., Huang,Z., Chen,X.-P., Zhang,B.-X. and Chu,L. (2019) Small nucleolar RNAs: insight into their function in cancer. *Front. Oncol.*, **9**, 587.
34. Lubelsky,Y. and Ulitsky,I. (2018) Sequences enriched in Alu repeats drive nuclear localization of long RNAs in human cells. *Nature*, **555**, 107–111.
35. Shukla,C.J., McCorkindale,A.L., Gerhardinger,C., Korthauer,K.D., Cabili,M.N., Shechner,D.M., Irizarry,R.A., Maass,P.G. and Rinn,J.L. (2018) High-throughput identification of RNA nuclear enrichment sequences. *EMBO J.*, **37**, e98452.
36. Matera,A.G. and Wang,Z. (2014) A day in the life of the spliceosome. *Nat. Rev. Mol. Cell Biol.*, **15**, 108–121.
37. Herzel,L., Ottoz,D.S.M., Alpert,T. and Neugebauer,K.M. (2017) Splicing and transcription touch base: co-transcriptional spliceosome assembly and function. *Nat. Rev. Mol. Cell Biol.*, **18**, 637–650.
38. Flynn,R.A., Almada,A.E., Zamudio,J.R. and Sharp,P.A. (2011) Antisense RNA polymerase II divergent transcripts are P-TEFb dependent and substrates for the RNA exosome. *Proc. Natl. Acad. Sci. U.S.A.*, **108**, 10460–10465.
39. Gallouzi,I.E. and Steitz,J.A. (2001) Delineation of mRNA export pathways by the use of cell-permeable peptides. *Science*, **294**, 1895–1901.
40. Chen,C.Y. and Shyu,A.B. (1995) AU-rich elements: characterization and importance in mRNA degradation. *Trends Biochem. Sci.*, **20**, 465–470.
41. Lebedeva,S., Jens,M., Theil,K., Schwanhausser,B., Selbach,M., Landthaler,M. and Rajewsky,N. (2011) Transcriptome-wide analysis of regulatory interactions of the RNA-binding protein HuR. *Mol. Cell*, **43**, 340–352.
42. Mukherjee,N., Corcoran,D.L., Nusbaum,J.D., Reid,D.W., Georgiev,S., Hafner,M., Ascano,M. Jr, Tuschl,T., Ohler,U. and Keene,J.D. (2011) Integrative regulatory mapping indicates that the RNA-binding protein HuR couples pre-mRNA processing and mRNA stability. *Mol. Cell*, **43**, 327–339.
43. Yi,J., Chang,N., Liu,X., Guo,G., Xue,L., Tong,T., Gorospe,M. and Wang,W. (2010) Reduced nuclear export of HuR mRNA by HuR is linked to the loss of HuR in replicative senescence. *Nucleic Acids Res.*, **38**, 1547–1558.
44. Ochs,R.L., Lischwe,M.A., Spohn,W.H. and Busch,H. (1985) Fibrillarin: a new protein of the nucleolus identified by autoimmune sera. *Biol. Cell*, **54**, 123–133.
45. Politz,J.C., Yarovoi,S., Kilroy,S.M., Gowda,K., Zwieb,C. and Pederson,T. (2000) Signal recognition particle components in the nucleolus. *Proc. Natl. Acad. Sci. U.S.A.*, **97**, 55–60.
46. Yu,Y.T., Shu,M.D., Narayanan,A., Terns,R.M., Terns,M.P. and Steitz,J.A. (2001) Internal modification of U2 small nuclear (sn)RNA occurs in nucleoli of Xenopus oocytes. *J. Cell Biol.*, **152**, 1279–1288.
47. Gerbi,S.A. and Lange,T.S. (2002) All small nuclear RNAs (snRNAs) of the [U4/U6.U5] Tri-snRNP localize to nucleoli; identification of the nucleolar localization element of U6 snRNA. *Mol. Biol. Cell*, **13**, 3123–3137.
48. Benoit Bouvrette,L.P., Cody,N.A.L., Bergalet,J., Lefebvre,F.A., Diot,C., Wang,X., Blanchette,M. and Lécuyer,E. (2018) CeFra-seq reveals broad asymmetric mRNA and noncoding RNA distribution profiles in *Drosophila* and human cells. *RNA*, **24**, 98–113.
49. Gandin,E., Lion,Y. and Van de Vorst,A. (1983) Quantum yield of singlet oxygen production by xanthene derivatives. *Photochem. Photobiol.*, **37**, 271–278.
50. Ruiz-González,R., Cortajarena,A.L., Mejias,S.H., Agut,M., Nonell,S. and Flors,C. (2013) Singlet oxygen generation by the genetically encoded tag miniSOG. *J. Am. Chem. Soc.*, **135**, 9564–9567.
51. Torra,J., Lafaye,C., Signor,L., Aumonier,S., Flors,C., Shu,X., Nonell,S., Gotthard,G. and Royant,A. (2019) Tailing miniSOG: structural bases of the complex photophysics of a flavin-binding singlet oxygen photosensitizing protein. *Sci. Rep.*, **9**, 1–10.
52. Endres,S., Wingen,M., Torra,J., Ruiz-González,R., Polen,T., Bosio,G., Bitzenhofer,N.L., Hilgers,F., Gensch,T., Nonell,S. *et al.* (2018) An optogenetic toolbox of LOV-based photosensitizers for light-driven killing of bacteria. *Sci. Rep.*, **8**, 1–14.
53. Hernandez-Verdun,D. (2011) Assembly and disassembly of the nucleolus during the cell cycle. *Nucleus*, **2**, 189–194.
54. Okamura,M., Inose,H. and Masuda,S. (2015) RNA Export through the NPC in Eukaryotes. *Genes*, **6**, 124–149.
55. Jang,B.-C., Muñoz-Najar,U., Paik,J.-H., Claffey,K., Yoshida,M. and Hla,T. (2003) Leptomycin B, an inhibitor of the nuclear export receptor CRM1, inhibits COX-2 expression. *J. Biol. Chem.*, **278**, 2773–2776.
56. Brennan,C.M., Gallouzi,I.E. and Steitz,J.A. (2000) Protein ligands to HuR modulate its interaction with target mRNAs in vivo. *J. Cell Biol.*, **151**, 1–14.
57. Sleeman,J. (2007) A regulatory role for CRM1 in the multi-directional trafficking of splicing snRNPs in the mammalian nucleus. *J. Cell Sci.*, **120**, 1540–1550.
58. Xiao,Z., Zou,Q., Liu,Y. and Yang,X. (2016) Genome-wide assessment of differential translations with ribosome profiling data. *Nat. Commun.*, **7**, 11194.
59. Bakheet,T., Hitti,E. and Khabar,K.S.A. (2018) ARED-Plus: an updated and expanded database of AU-rich element-containing mRNAs and pre-mRNAs. *Nucleic Acids Res.*, **46**, D218–D220.
60. Peng,S.S., Chen,C.Y., Xu,N. and Shyu,A.B. (1998) RNA stabilization by the AU-rich element binding protein, HuR, an ELAV protein. *EMBO J.*, **17**, 3461–3470.
61. Gallouzi,I.E., Brennan,C.M. and Steitz,J.A. (2001) Protein ligands mediate the CRM1-dependent export of HuR in response to heat shock. *RNA*, **7**, 1348–1361.

62. Shaw,G. and Kamen,R. (1986) A conserved AU sequence from the 3′ untranslated region of GM-CSF mRNA mediates selective mRNA degradation. *Cell*, **46**, 659–667.
63. Johnson,B.A., Stehn,J.R., Yaffe,M.B. and Blackwell,Keith,T. (2002) Cytoplasmic localization of tristetraprolin involves 14-3-3-dependent and -independent mechanisms. *J. Biol. Chem.*, **277**, 18029–18036.
64. Ciolli Mattioli,C., Rom,A., Franke,V., Imami,K., Arrey,G., Terne,M., Woehler,A., Akalin,A., Ulitsky,I. and Chekulaeva,M. (2019) Alternative 3′ UTRs direct localization of functionally diverse protein isoforms in neuronal compartments. *Nucleic Acids Res.*, **47**, 2560–2573.
65. Goering,R., Hudish,L.I., Guzman,B.B., Raj,N., Bassell,G.J., Russ,H.A., Dominguez,D. and Taliaferro,J.M. (2020) FMRP promotes RNA localization to neuronal projections through interactions between its RGG domain and G-quadruplex RNA sequences. *Elife*, **9**.
66. Miyamichi,K., Amat,F., Moussavi,F., Wang,C., Wickersham,I., Wall,N.R., Taniguchi,H., Tasic,B., Josh Huang,Z., He,Z. *et al.* (2010) Cortical representations of olfactory input by trans-synaptic tracing. *Nature*, **472**, 191–196.
67. Wolff,B., Sanglier,J.J. and Wang,Y. (1997) Leptomycin B is an inhibitor of nuclear export: inhibition of nucleo-cytoplasmic translocation of the human immunodeficiency virus type 1 (HIV-1) Rev protein and Rev-dependent mRNA. *Chem. Biol.*, **4**, 139–147.